

Boise State University

ScholarWorks

---

Materials Science and Engineering Faculty  
Publications and Presentations

Micron School for Materials Science and  
Engineering

---

9-2023

## Intrinsic and Atomic Layer Etching Enhanced Area-Selective Atomic Layer Deposition of Molybdenum Disulfide Thin Films

Jake Soares

*Boise State University*

Wesley Jen

*Boise State University*

John D. Hues

*Boise State University*

Drew Lysne

*Boise State University*

Jesse Wensel

*Micron Technology*

*See next page for additional authors*

---

### Publication Information

Soares, Jake; Wesley, Jen; Hues, John D.; Lysne, Drew; Wensel, Jesse; Hues, Steven M.; and Graugnard, Elton. (2023). "Intrinsic and Atomic Layer Etching Enhanced Area-Selective Atomic Layer Deposition of Molybdenum Disulfide Thin Films". *Journal of Vacuum Science and Technology A*, 41(5), 052404.

<https://doi.org/10.1116/6.0002811>

This article may be downloaded for personal use only. Any other use requires prior permission of the author and AIP Publishing. This article appeared in:

Soares, J.; Wesley, J.; Hues, J.D.; Lysne, D.; Wensel, J.; Hues, S.M.; and Graugnard, E. (2023). Intrinsic and atomic layer etching enhanced area-selective atomic layer deposition of molybdenum disulfide thin films. *Journal of Vacuum Science and Technology A*, 41(5), 052404. <https://doi.org/10.1116/6.0002811>

and may be found at <https://doi.org/10.1116/6.0002811>.

---

**Authors**

Jake Soares, Wesley Jen, John D. Hues, Drew Lysne, Jesse Wensel, Steven M. Hues, and Elton Graugnard

# Intrinsic and Atomic Layer Etching Enhanced Area-Selective Atomic Layer Deposition of Molybdenum Disulfide Thin Films

Jake Soares<sup>1</sup>, Wesley Jen<sup>1</sup>, John D. Hues<sup>1</sup>, Drew Lysne<sup>1</sup>, Jesse Wensel<sup>2</sup>, Steven M. Hues<sup>1</sup>, Elton Graugnard<sup>1,3,a)</sup>

<sup>1</sup> Micron School of Materials Science and Engineering, Boise State University, 1910 University Dr., Boise, ID 83725, USA

<sup>2</sup> Micron Technology, 8000 S Federal Way, Boise, ID, 83707, USA

<sup>3</sup> Center for Advanced Energy Studies, Idaho Falls, ID 83401, USA

a) Electronic mail: [eltongraugnard@boisestate.edu](mailto:eltongraugnard@boisestate.edu)

For continual scaling in microelectronics, new processes for precise high volume fabrication are required. Area-selective atomic layer deposition (ASALD) can provide an avenue for self-aligned material patterning and offers an approach to correct for edge placement errors commonly found in top-down patterning processes. Two-dimensional transition metal dichalcogenides (TMDs) also offer great potential in scaled microelectronic devices due to their high mobilities and few-atom thickness. In this work, we report ASALD of MoS<sub>2</sub> thin films by deposition with MoF<sub>6</sub> and H<sub>2</sub>S precursor reactants. The inherent selectivity of the MoS<sub>2</sub> atomic layer deposition (ALD) process is demonstrated by growth on common dielectric materials in contrast to thermal oxide/ nitride substrates. The selective deposition produced few layer MoS<sub>2</sub> films on patterned growth regions as measured by Raman spectroscopy and time-of-flight secondary ion mass spectrometry. We additionally demonstrate that the selectivity can be enhanced by implementing atomic layer etching (ALE) steps at regular intervals during MoS<sub>2</sub> growth. This area-selective ALD process provides an approach for integrating 2D films into next-generation devices by leveraging the

ACCEPTED MANUSCRIPT  
This is the author's peer reviewed, accepted manuscript. However, the online version of record will be different from this version once it has been copyedited and typeset.  
PLEASE CITE THIS ARTICLE AS DOI: 10.1116/6.0002811

inherent differences in surface chemistries and providing insight in the effectiveness of a supercycle ALD and ALE process.

## I. INTRODUCTION

As feature sizes shrink, the need for precise patterning methods is critical. Commonly, top-down approaches to nanoscale processing are used to pattern features in high volume manufacturing (HVM) of semiconductor devices. These include photolithography,<sup>1,2,3</sup> and other soft-lithography techniques<sup>4,5</sup> followed by dry etching,<sup>6</sup> wet etching,<sup>7</sup> or deposition. These methods have been a standard in semiconductor manufacturing; however, as dimensions scale below the 7 nm node,<sup>8</sup> new techniques need to be developed to correct for misalignment issues.<sup>9</sup> At the nanoscale, pattern misalignments can have a drastic impact on device performance and even lead to device failure. This issue is only exacerbated when the number of processing steps, comprising further patterning and deposition, build upon the misaligned underlying layer.

Area-selective atomic layer deposition (ASALD) can mitigate alignment errors by providing a bottom-up approach to selectively deposit films on predetermined areas.<sup>10</sup> This method uses the differences in surface chemistry between growth (GA) and non-growth (NGA) areas to deposit primarily on surfaces that promote nucleation. ALD is a technique that employs self-limiting surface chemical reactions for thin film growth. While sometimes valued as a deposition process that produces continuous, pinhole-free conformal thin films,<sup>11</sup> that deposition behavior relies on uniform surface chemistry to promote uniform film nucleation. However, by exploiting the differences in surface chemistry, preferential nucleation can promote selectivity during deposition.<sup>12</sup>

Several methods have been reported to enable ASALD.<sup>13</sup> Self-assembled monolayers (SAMs) have been shown to promote selectivity by selectively functionalizing (or

defunctionalizing) a specific area on a pre-patterned substrate.<sup>14-16</sup> SAMs achieve this selectivity due to the tail group (functionalized group) of the monolayer, which blocks precursor chemisorption on the substrate surface. Precursor choice also influences ALD selectivity by means of ligand reactivity and ligand size, as shown in the selective deposition of Al<sub>2</sub>O<sub>3</sub> on SiO<sub>2</sub>.<sup>17</sup> This method is useful for defining both growth and non-growth regions; however, it typically relies on a wet chemistry and long exposures for SAM placement and ordering. Using small molecule inhibitors that selective bind to patterned regions can yield ASALD processes where the inhibitor exposure can form a third step in an ALD cycle.<sup>18</sup> Lastly, selective deposition can be achieved by exploiting inherent substrate selectivity based on substrate functional groups. Some of these methods rely on precursor adsorption reactivity.<sup>19, 20</sup> This approach has been demonstrated by the implementation and control over nucleation islands for selective plasma-enhanced ALD of WS<sub>2</sub> and by control over the density of hydroxyl (OH) groups on SiO<sub>2</sub> surfaces for the selective deposition of MoS<sub>2</sub>.<sup>21, 22, 23</sup> These processes require use of a pre-patterning step for seed or OH placement, for example, using either O<sub>2</sub> plasma<sup>21</sup> or ion beam patterning.<sup>22</sup> To our knowledge there has been only one other ASALD report of selective deposition of MoS<sub>2</sub> films by use of assisted etching during deposition. Ahn *et al.* has demonstrated the ASALD of MoS<sub>2</sub> by MoCl<sub>5</sub> adsorption and subsequent self-etching effect for selective MoS<sub>2</sub> deposition on Al patterns versus SiO<sub>2</sub>.<sup>24</sup>

In this work, we report area-selective ALD of MoS<sub>2</sub> thin films by deposition with MoF<sub>6</sub> and H<sub>2</sub>S reactants. The inherent differences in surface groups between common ALD-deposited metal oxide surfaces and thermal oxide/nitride substrates leads to the selective nucleation and deposition of MoS<sub>2</sub> films on the metal oxide regions. Initial screening of substrate materials by X-ray photoelectron spectroscopy (XPS) identified materials that either promoted or inhibited

nucleation of MoS<sub>2</sub> after a range of MoS<sub>2</sub> cycles. Selectivity parameters were calculated between growth and non-growth surfaces. Substrate templates were then pre-pattered with both growth and non-growth areas to verify the selective MoS<sub>2</sub> process. Time-of-flight secondary ion mass spectrometry (ToF-SIMS) and Raman mode line maps confirmed selective MoS<sub>2</sub> deposition on growth regions of the template substrates. Further, selectivity was enhanced by integrating atomic layer etching steps during ALD.

## II. EXPERIMENTAL

### A. MoS<sub>2</sub> deposition

ALD growth of MoS<sub>2</sub> films were performed in custom viscous flow reactor following the process reported previously.<sup>25</sup> Briefly, the process pressure was held constant at ~1 Torr by flowing 125 sccm of ultra-high purity nitrogen (99.99% Norco) as a carrier gas. Reactor temperatures were held at 200 °C. MoS<sub>2</sub> ALD process followed typical dosing scheme of t<sub>1</sub>-t<sub>2</sub>-t<sub>3</sub>-t<sub>4</sub>, where exposure times are in seconds. t<sub>1</sub> and t<sub>2</sub> denote the molybdenum hexafluoride (molybdenum(VI) fluoride, Fisher Scientific) dose and purge times. t<sub>3</sub> and t<sub>4</sub> denote the H<sub>2</sub>S (hydrogen Sulfide, 99.5+%, Millipore Sigma) dose and purge times. Partial pressures of reactants for each dose were 60 mTorr for MoF<sub>6</sub> and 400 mTorr for H<sub>2</sub>S. Due to the high pressures of H<sub>2</sub>S, a regulator set at 1 ATM, and 200 μm orifice was placed on the H<sub>2</sub>S manifold delivery line.

Coupon substrates for MoS<sub>2</sub> ALD consisted of Si(100) with a native oxide or with an ALD dielectric coating. Deposited dielectrics consisted of alumina (Al<sub>2</sub>O<sub>3</sub>), hafnia (HfO<sub>2</sub>), and titania (TiO<sub>2</sub>) using trimethylaluminum (TMA, Millipore Sigma), tetrakis(dimethylamido)hafnium(IV) (TDMAH, 98% (99.99%-Hf), Millipore Sigma), and titanium tetrachloride (TiCl<sub>4</sub>, 99.995%, Millipore Sigma), respectively. For each dielectric, the oxygen source was water. Other coupon substrates included a 300 nm thermal SiO<sub>2</sub> (University

Wafer) and SiN and SiO<sub>x</sub>N<sub>y</sub> substrates (Micron Technology). Prior to any deposition, samples were sonicated for 1 min in acetone and 1 min in ethanol and then rinsed in Nanopure water. Lastly, samples were subject to a plasma glow discharge chamber for 30 seconds at a pressure of ~2 Torr in air to remove residual hydrocarbons.

Template substrates were patterned through standard photolithography. Coupons of doped silicon with 300 nm thermal oxide SiO<sub>2</sub> or SiO<sub>x</sub>N<sub>y</sub> were cleaved and cleaned with acetone and ethanol to remove any debris or contaminants during the cleaving process. The substrates were then placed on a spin-coater and coated with hexamethyldisilazane (HDMS) as a photoresist adhesion promoter and SPR220 3.0 (Megaposit) as the photoresist. A soft-bake at 115 °C for 90 seconds was conducted following each coating step. The coated substrates were aligned to a photomask and exposed using a Quintel Q-4000 Contact Aligner. The samples were subsequently developed using a photoresist developer (TMAH, Megaposit MF-26A) and rinsed with deionized water. Once dry, the patterned samples were placed in a GEMStar XT thermal ALD system (Arradiance) for deposition of a metal oxide film. Once the metal oxide was deposited, the photoresist was removed by sonicating the template substrate in acetone, followed by the cleaning process described earlier.

## B. Characterization

X-ray photoelectron spectroscopy (XPS) measurements were performed using a Physical Electronics (PHI) 5600 ESCA system using a monochromated Al K-alpha source with an analysis area of 3 mm × 10 mm. Survey scans used a pass energy of 200 eV and step size of 1 eV. High resolution scans used a pass energy of 50 eV and step size of 0.1 eV. The XPS data were analyzed using MultiPak 9.6. All spectra were referenced to the 1s peak (284.8 eV) of



adventitious carbon. Peak fitting of all high-resolution scans utilized a Shirley background to define the baseline. Region bounds were chosen such that bounds encompassed the totality of peaks present and were extended as far as possible without overlapping with other chemical peaks nearby. A Gaussian-Lorentzian peak mix was used when fitting spectra.

Raman spectroscopy was conducted on a Horiba LabRAM system in reflection mode. A 532 nm excitation laser, using a 100× aperture was used to probe samples. A neutral density filter setting ranging from 25% was used to prevent damage to the MoS<sub>2</sub> samples. Spectra were acquired over the 360-440 cm<sup>-1</sup> range to capture crystalline MoS<sub>2</sub> modes. Line scans were analyzed over the range of 395-415 cm<sup>-1</sup> to capture the MoS<sub>2</sub> A<sub>1g</sub> peak area.

Atomic force microscopy measurements (AFM) were performed on a MultiMode 8 (Bruker) operating in PeakForce-QNM mode. ScanAsyst-Air-HR probes (Bruker) with a tip radius of 2 nm were used for imaging. Image processing was carried out in NanoScope Analysis 2.0.

In this work, ToF-SIMS images were acquired by measuring the intensity of each analyte, at given mass/charge, at each pixel to provide a distribution of the analyte across the surface. Analyses were performed in positive secondary ion mode using a 25 keV Bi<sup>1+</sup> primary ions beam rastered over a 200 × 200 μm<sup>2</sup> area with an original image pixel density of 512 × 512, images were then binned to 128 × 128, post analysis, to improve contrast.

### III. RESULTS AND DISCUSSION

#### A. Material screening

Initial screening of various substrate materials was experimentally conducted to identify substrates that promoted or inhibited MoS<sub>2</sub> growth. We expected that substrates with larger hydroxyl (OH) concentrations would promote deposition compared to substrates that have strong



surface bonding and lack reactive surface groups. Our previous studies have shown a temperature dependence for MoF<sub>6</sub> precursor adsorption, which we attribute to differences in relative hydroxyl concentrations.<sup>26</sup> These studies suggest that increased OH concentrations promote increases in MoF<sub>6</sub> chemisorption on metal oxide surfaces. Moreover, Lawson *et al.* reported density functional theory calculations describing the nucleation behavior of MoF<sub>6</sub> precursors on hydroxylated and non-hydroxylated metal oxide surfaces.<sup>27</sup> They reported a higher reactivity and subsequent chemisorption of the MoF<sub>6</sub> precursor towards the hydroxylated metal oxides compared to a weak interaction with non-hydroxylated metal oxide surfaces.

To experimentally screen surfaces for MoS<sub>2</sub> nucleation, XPS spectra were acquired for planar coupon substrate materials after MoS<sub>2</sub> ALD. Each material substrate was exposed to 22 MoS<sub>2</sub> ALD cycles followed by annealing at 650 °C in H<sub>2</sub>S for 30 min. After deposition, high-resolution Mo 3d XPS scans were captured (Fig. 1). The spectra are offset vertically for ease of viewing. The relative intensities of the spectra were used to determine which material surfaces promoted or delayed MoS<sub>2</sub> nucleation. Based on these preliminary experiments, thermal SiO<sub>2</sub> (TO) and SiO<sub>x</sub>N<sub>y</sub> had the lowest concentration of Mo compared to the metal oxides, such as Al<sub>2</sub>O<sub>3</sub> and HfO<sub>2</sub>, that showed greater Mo 3d peak intensities.

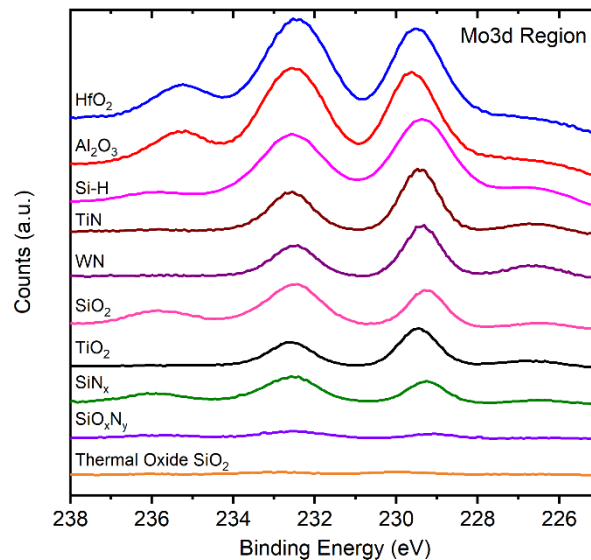


FIG. 1. X-ray photoelectron spectroscopy scans on a variety of substrate surfaces measuring photo-emitted electron intensities in the Mo 3d region after 22 MoS<sub>2</sub> cycles at 200 °C and annealing at 650 °C for 30 min. Spectra are offset vertically for clarity. These data enable identification of surfaces that either promote (HfO<sub>2</sub> and Al<sub>2</sub>O<sub>3</sub>) or inhibit (SiN<sub>x</sub>, SiO<sub>x</sub>N<sub>y</sub> and thermal oxide SiO<sub>2</sub>) MoS<sub>2</sub> nucleation.

Based on the XPS data, additional experiments were conducted to measure the selectivity between the surfaces that exhibited large differences in Mo concentration. ALD Al<sub>2</sub>O<sub>3</sub> and HfO<sub>2</sub> were identified as materials that promoted MoS<sub>2</sub> growth, while SiN<sub>x</sub>, SiO<sub>x</sub>N<sub>y</sub>, and TO were seen as substrates that delayed nucleation. ALD MoS<sub>2</sub> was performed on planar coupons of the respective substrate materials. After 5-20 MoS<sub>2</sub> ALD cycles, high-resolution XPS scans were taken on the coupons over the Mo 3d region. Peak fitting of the spectra within the Mo 3d region was conducted to calculate the integrated area. These calculations excluded the overlapping S 2s peak area. Figure 2 shows the Mo peak area versus the number of ALD cycles for each substrate. A clear Mo nucleation delay can be seen for the TO (squares), SiN<sub>x</sub> (diamonds), and SiO<sub>x</sub>N<sub>y</sub> substrates (inverted triangles) compared to the metal oxides Al<sub>2</sub>O<sub>3</sub> (circles) and HfO<sub>2</sub> (triangles).



This is the author's peer reviewed, accepted manuscript. However, the online version of record will be different from this version once it has been copyedited and typeset.

PLEASE CITE THIS ARTICLE AS DOI: 10.1116/6.0002811

This is an author-produced, peer-reviewed version of this article. The final, definitive version of this document can be found online at *Journal of Vacuum Science and Technology A*, published by American Institute of Physics. Copyright restrictions may apply. <https://doi.org/10.1116/6.0002811>

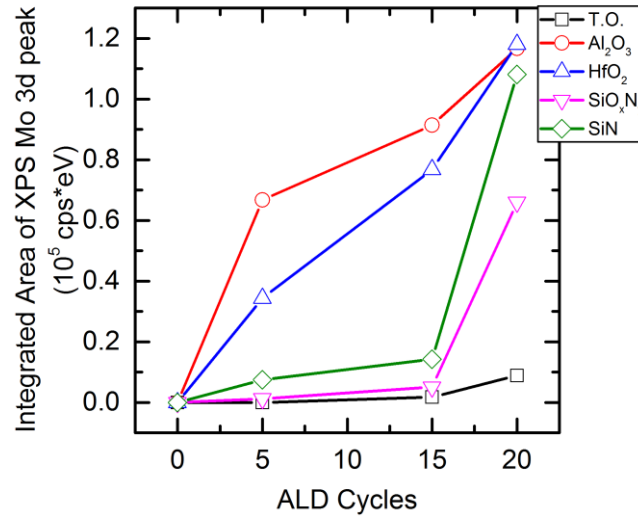


FIG. 2. Integrated area of XPS Mo 3d peak region as a function of MoS<sub>2</sub> ALD cycles for a variety of substrates. All substrates were prepared with 20 cycles of MoS<sub>2</sub> ALD at 200 °C. Integrated area was calculated after peak fitting the Mo 3d region (excluding the overlapping S 2s spectra).

From the XPS results of the Mo 3d integrated peak area, the selectivity between the growth and non-growth areas was calculated using Equation 1. The selectivity is based on the amount of material present after deposition on growth areas ( $\theta_{GA}$ ) and non-growth areas ( $\theta_{NGA}$ ).<sup>28</sup>

$$Selectivity = \frac{\theta_{GA} - \theta_{NGA}}{\theta_{GA} + \theta_{NGA}} \quad (1)$$

Figure 3 shows the calculated selectivity values as a function of ALD cycles between identified growth and non-growth surfaces. The Al<sub>2</sub>O<sub>3</sub> and TO had the greatest Mo concentration differences. After 5 MoS<sub>2</sub> cycles there was a high selectivity value of  $S = \sim 1$ . Essentially no Mo was detected on the TO surface by XPS. The selectivity was calculated to be  $S = 0.96$  at 15 cycles and decreased to  $S = 0.85$  at 20 ALD cycles. Beyond 20 cycles, the selectivity dropped dramatically to  $S = 0.51$  for 30 ALD cycles.

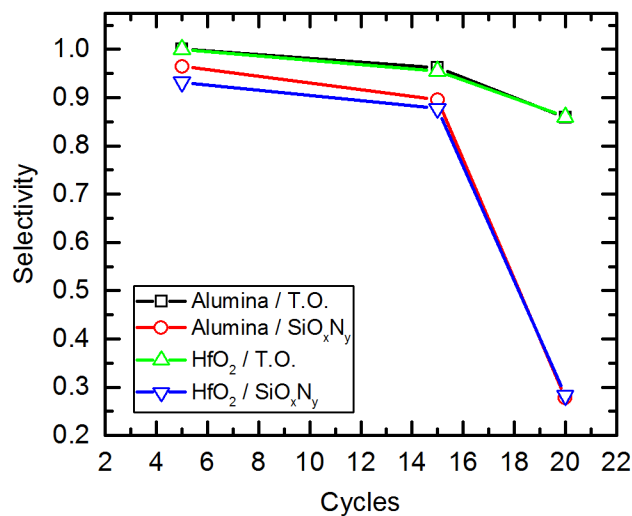


FIG. 3. Calculated selectivity parameter as a function of MoS<sub>2</sub> ALD cycles at 200 °C for blanket substrates that promote or inhibit MoS<sub>2</sub> growth. The selectivity was calculated based on integrated XPS Mo concentrations.

The high selectivity observed between the Al<sub>2</sub>O<sub>3</sub> and the TO is expected due to relative concentrations of surface OH groups. It has been reported that ALD alumina films (deposited with TMA and H<sub>2</sub>O) contain high concentrations of OH groups throughout the film<sup>29</sup> and are the terminating groups left on the surface after deposition (H<sub>2</sub>O as last precursor dose).<sup>30</sup> Studies have also experimentally calculated the hydroxyl coverage on the alumina surface and is expected to be ~9 nm<sup>-2</sup> at 200 °C.<sup>31</sup> Comparatively, thermal oxide only has ~1.5-3 nm<sup>-2</sup> OH group coverage.<sup>32</sup> This stark difference in OH concentration supports the observed selectivity between the TO and Al<sub>2</sub>O<sub>3</sub> surfaces. Thermal oxide has also been shown to be relatively resistant to WF<sub>6</sub> nucleation during W chemical vapor deposition (CVD) and ALD reactions.<sup>33, 34</sup> In studies of selective W deposition, the presence of Si-OH groups was shown to contribute to nucleation on the non-growth SiO<sub>2</sub> surface. The fluorination on the SiO<sub>2</sub> surface can also play a role in either promoting or inhibiting nucleation<sup>33</sup> and can contribute to etching of SiO<sub>2</sub>, which can extend selectivity.<sup>34</sup> To determine whether fluorination was inhibiting nucleation on the TO

surface, we performed 10 cycles of MoS<sub>2</sub> ALD, with no annealing, on ALD alumina, thermal SiO<sub>2</sub>, and native SiO<sub>2</sub> cleaned in fuming sulfuric acid. The concentrations of Mo, S, and F are provided in the Supplemental Material (SM) at [URL will be inserted by AIP Publishing]. The alumina and native SiO<sub>2</sub> exhibit Mo and S content, indicating nucleation, and fluorine content is expected from residual fluorine within the unannealed films. However, the thermal SiO<sub>2</sub> exhibited negligible Mo and S content. The results indicate a small level of fluorination from the MoF<sub>6</sub> exposures to the TO substrate, but additional studies are needed to evaluate whether this fluorine is inhibiting the nucleation of Mo or whether the Mo nucleation is inhibited primarily by the lack of hydroxyl groups.

## B. ASALD on Templates

To further explore the selective process, template surfaces were created that contained both a growth area and non-growth area. TO, SiN<sub>x</sub>, and SiO<sub>x</sub>N<sub>y</sub> substrates were patterned with ALD Al<sub>2</sub>O<sub>3</sub>, HfO<sub>2</sub> or TiO<sub>2</sub> using photolithography. Templates were then exposed to 20 MoS<sub>2</sub> ALD cycles at 200 °C followed by annealing at 650 °C in H<sub>2</sub>S for 30 min to form crystalline films.<sup>35</sup> The samples were then characterized by Raman spectroscopy to probe the selectivity of the deposition process.

Raman point scans were captured on and off the growth regions for each template substrate. See the SM for additional Raman mode line scans and ToF-SIMS maps. Figure S1 in the SM shows the results of point scans on Al<sub>2</sub>O<sub>3</sub>/TO and Al<sub>2</sub>O<sub>3</sub>/SiO<sub>x</sub>N<sub>y</sub> templates. Characteristic E<sub>2g</sub><sup>1</sup> and A<sub>1g</sub> modes<sup>36</sup> for crystalline MoS<sub>2</sub> were identified on the growth region (Al<sub>2</sub>O<sub>3</sub>) for both template substrates. These modes can be identified at ~380 and 405 cm<sup>-1</sup>. No modes were observed on the non-growth TO regions, while a slight emergence of the A<sub>1g</sub> mode on the

SiO<sub>x</sub>N<sub>y</sub> non-growth region was observed. With the initial results from point scans, Raman line scans of the A<sub>1g</sub> mode intensity were conducted across a ~10 μm growth area feature for all templates. The line scans spanned far enough to include regions of the non-growth areas (TO or SiO<sub>x</sub>N<sub>y</sub>). These Raman line scans are shown in Figure 4(a). An optical image of an Al<sub>2</sub>O<sub>3</sub> / TO sample is shown in Figure 4(b). The annotated dashed line represents where the line scan was taken across the template substrate. All templates show great contrast between the growth and non-growth regions revealing a high A<sub>1g</sub> intensity within the growth areas only. For all patterned growth areas, the Raman A<sub>1g</sub> mode intensity was roughly ~2 orders of magnitude larger than compared to the TO substrate. The morphology of the interface between the Al<sub>2</sub>O<sub>3</sub> and TO regions was investigated using AFM following 20 cycles of MoS<sub>2</sub> ALD and annealing in H<sub>2</sub>S for 30 min at 650 °C. Figure S3 shows greater deposition on the Al<sub>2</sub>O<sub>3</sub> region but also reveals MoS<sub>2</sub> nuclei forming on the TO region. We attribute the eventual loss of selectivity to the coalescence of the MoS<sub>2</sub> nuclei in the TO region with additional ALD cycles.

The selectivity was also probed on SiO<sub>x</sub>N<sub>y</sub> and SiN<sub>x</sub> substrates patterned with ALD Al<sub>2</sub>O<sub>3</sub>. These also show a degree of selectivity, although it is not as pronounced as the Al<sub>2</sub>O<sub>3</sub>/TO. This result can be expected as the previous XPS data indicates a lower calculated selectivity with addition to the slight emergence of the A<sub>1g</sub> mode captured in the Raman point scan. The Raman data for the templates prepared with SiO<sub>x</sub>N<sub>y</sub> and SiN<sub>x</sub> can be found in the SM.

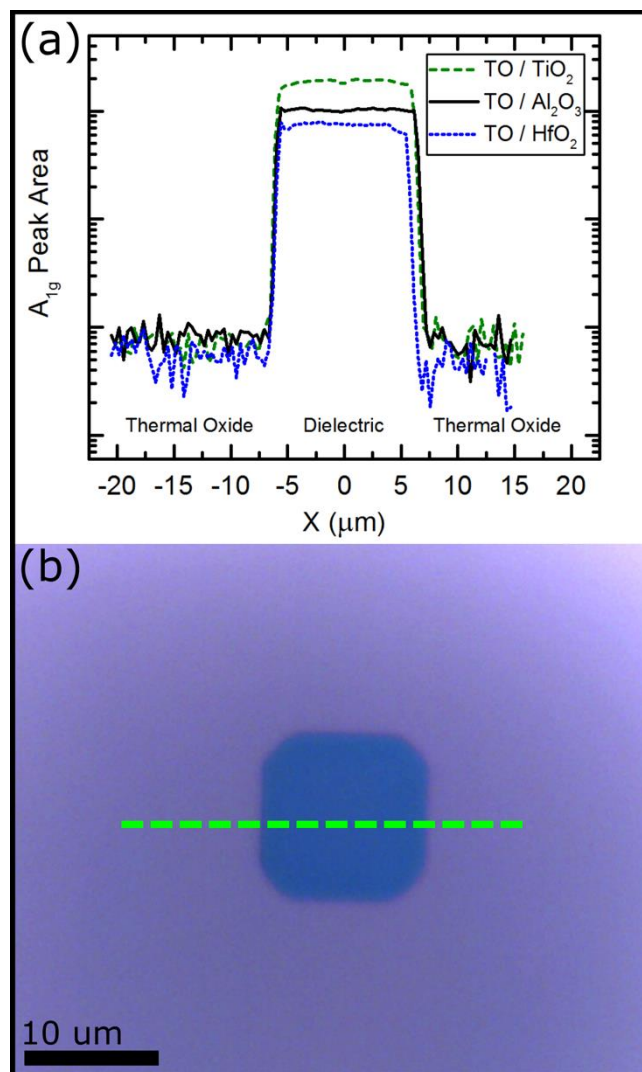


FIG. 4. (a) Raman line scans across the template substrates containing both growth and non-growth regions. Intensity is measured by crystalline  $\text{MoS}_2$   $A_{1g}$  peak area. Clear indication of crystalline  $\text{MoS}_2$  can be identified on all growth areas. (b) Example optical image of a patterned  $\text{Al}_2\text{O}_3$  / TO region. The dashed line approximates the region of the line scan across the template. Samples were prepared with 20 cycles of  $\text{MoS}_2$  ALD at 200  $^\circ\text{C}$  followed by annealing in  $\text{H}_2\text{S}$  at 650  $^\circ\text{C}$  for 30 min.

To further characterize the selectivity of the ASALD process, time-of-flight secondary ion mass spectrometry (ToF-SIMS) elemental maps of template substrates were acquired.

Template substrates for these measurements were made of either TO or  $\text{SiO}_x\text{N}_y$  substrates patterned with ALD  $\text{Al}_2\text{O}_3$ . Templates were prepared with 20 cycles of  $\text{MoS}_2$  ALD at  $200^\circ\text{C}$  and were annealed at  $650^\circ\text{C}$  in  $\text{H}_2\text{S}$  for 30 min. to form a crystalline film. Figure 5 shows the  $\text{Mo}^+$ ,  $\text{SiOH}^+$ , and  $\text{Al}^+$  elemental channels from ToF-SIMS analysis. The intensity describes the elemental (mass/charge) concentration of the listed species. Both growth and non-growth regions can easily be identified by the relative color scale of the respective ion species. The  $\text{Mo}^+$  channel clearly distinguishes the selectivity of the molybdenum species on the  $\text{Al}_2\text{O}_3$  growth area. Where the  $\text{Mo}^+$  intensity is greatest within the central growth area and near zero on the surrounding TO substrate. ToF-SIMS maps showing similar results for selective deposition on the  $\text{Al}_2\text{O}_3/\text{SiO}_x\text{N}_y$  patterned samples can be found in the SM.

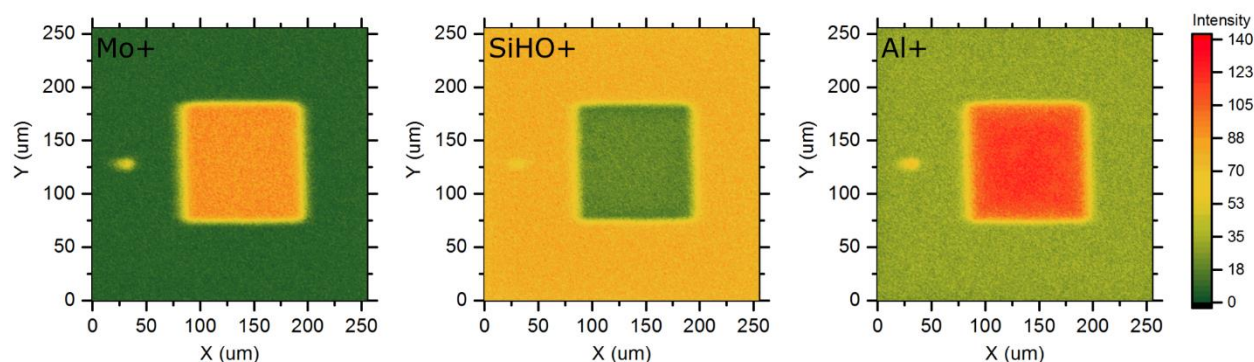


FIG. 5. Time-of-flight secondary ion mass spectrometry maps of alumina / TO template following 20  $\text{MoS}_2$  ALD cycles at  $200^\circ\text{C}$ . Maps show clear selectivity of Mo within the patterned alumina growth area. Essentially no Mo is present on the non-growth thermal oxide area.

### C. Etching Enhanced ASALD of $\text{MoS}_2$

Recently, several groups have reported the successful combination of ASALD and selective etching to improve process selectivity.<sup>37-40</sup> These works integrate etching steps within



the ALD process to suppress the nucleation that occurs on the non-growth areas. By incorporating intermittent etching steps during ALD, the selectivity between the growth and non-growth areas can effectively be extended. We have previously reported an atomic layer etching (ALE) process for MoS<sub>2</sub> thin films.<sup>41</sup> This ALE process utilizes the sequential exposure of MoF<sub>6</sub> and H<sub>2</sub>O precursors for MoS<sub>2</sub> film removal. This ALE process was incorporated to extend the selectivity of the MoS<sub>2</sub> ASALD process.

Deposition enhanced by etching was investigated on blanket planar coupons of Al<sub>2</sub>O<sub>3</sub> and TO. We implemented supercycle recipes for these experiments, where one supercycle is defined as a number of ALD cycles followed by a number of ALE cycles. At intervals of every 10 ALD cycles, 30 cycles of etching were performed, comprising one supercycle. A total of 2-3 supercycles were conducted on the coupon substrates to test the etching assisted ASALD process.

The integrated area of XPS Mo 3d data shows a much lower Mo concentration after 20 and 30 ALD cycles for deposition that implemented a supercycle recipe as compared to the standard ASALD process (Fig. 6). The resulting selectivity was calculated for the experiments utilizing supercycle recipes producing  $S_{(SC\ x2)} = 0.95$  and  $S_{(SC\ x3)} = 0.92$  after a total of 20 and 30 ALD cycles, respectively. These data suggest that implementing a dep-etch supercycle recipe can suppress Mo nucleation on the non-growth region over an extended range of ALD cycles. This result can be implemented to obtain a much more selective deposition process by reducing any formed nuclei on the non-growth region, and aid in the selective deposition of thicker MoS<sub>2</sub> films.

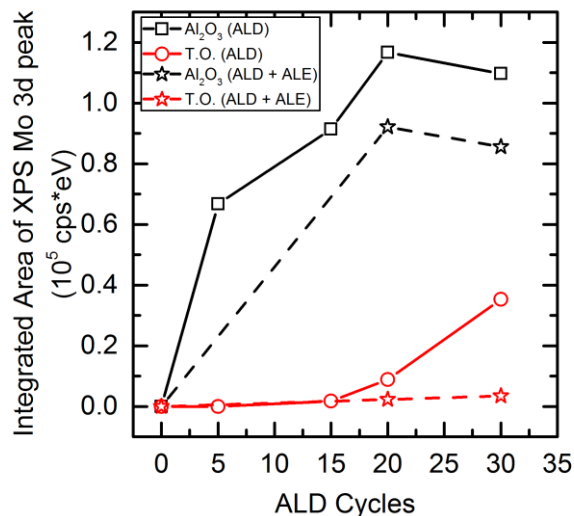


FIG. 6. Integrated area of XPS Mo 3d peak region as a function of total MoS<sub>2</sub> ALD cycles for thermal oxide and Al<sub>2</sub>O<sub>3</sub> substrates. The incorporation of etching steps is shown to decrease the amount of Mo present after a total of 20 and 30 ALD cycles. Dashed lines indicate growth that integrated supercycles of deposition and etching. Solid lines indicate ASALD without ALE supercycles.

#### IV. CONCLUSIONS

In this work, we report the ASALD of MoS<sub>2</sub> films. Initial screening of common semiconductor surfaces including metal oxides and silicon oxide/nitride was conducted by XPS measurements. A nucleation delay was observed on thermal SiO<sub>2</sub> and SiN<sub>x</sub> and SiO<sub>x</sub>N<sub>y</sub> substrates compared to Al<sub>2</sub>O<sub>3</sub> and HfO<sub>2</sub>. This nucleation delay is attributed to a difference in inherent hydroxyl concentrations between the surfaces, which impacts the nucleation of the MoF<sub>6</sub> precursor. The selectivity parameter was calculated between substrates that delayed nucleation and promoted nucleation. A selectivity between thermal SiO<sub>2</sub> and Al<sub>2</sub>O<sub>3</sub> was calculated to be  $S = 0.85$  after 20 ALD cycles. Time-of-flight SIMS and Raman line scans confirmed the ASALD process of MoS<sub>2</sub> on pre-patterned template substrates of Al<sub>2</sub>O<sub>3</sub> and thermal SiO<sub>2</sub>. The selectivity of our ASALD process was improved by implementing atomic layer etching steps during ALD. This combination of

deposition and etching extended the total number of ALD cycles that could be performed while improving the selectivity between surfaces. This work will help realize the potential for area-selective ALD by utilizing inherent differences in substrate surface chemistry. Additionally, this study demonstrates processing methods that can be used for MoS<sub>2</sub> integration in manufacturing and offers an approach to bottom-up, self-aligned fabrication.

## ACKNOWLEDGMENTS

We would like to thank members of the Atomic Films Lab for valuable discussions. We thank Icelene Leong for valuable assistance with the XPS studies. We thank Scott Sills at Micron Technology for providing coated wafers for blanket studies. Atomic force microscopy was performed in the Surface Science Laboratory at Boise State University. This work was supported in part by National Science Foundation CAREER grant no. 1751268 and the National Science Foundation Center for Atomically Thin Multifunctional Coatings (ATOMIC) IUCRC (grant no. 2113873).

## AUTHOR DECLARATIONS

### **Conflict of Interest**

The authors have no conflicts to disclose.

## SUPPLEMENTAL MATERIAL

Supplemental material at [URL will be inserted by AIP Publishing] for additional Raman spectra, an atomic force micrograph at a template edge, additional ToF-SIMS maps, and additional XPS data.

## DATA AVAILABILITY

The data that support the described findings are available within the primary article and the supplemental material.

## REFERENCES

1. G. E. Moore, presented at the Integrated Circuit Metrology, Inspection, and Process Control IX, (1995).
2. R. Seisyan, *Technical Physics* 56 (8), 1061-1073 (2011).
3. A. Pimpin and W. Srituravanich, *Engineering Journal* 16 (1), 37-56 (2012).
4. Y. Xia and G. M. Whitesides, *Annual Review of Materials Science* 28 (1), 153-184 (1998).
5. F. Wisser, B. Schumm, G. Mondin, J. Grothe and S. Kaskel, *Journal of Materials Chemistry C* 3 (12), 2717-2731 (2015).
6. K. Nojiri, *Dry Etching Technology for Semiconductors*. (Springer, 2015).
7. J. C. Love, K. E. Paul and G. M. Whitesides, *Adv. Mater.* 13 (8), 604-607 (2001).
8. A. Pandey, *Silicon*, 1-12 (2022).
9. R. Clark, K. Tapily, K.-H. Yu, T. Hakamata, S. Consiglio, D. O'Meara, C. Wajda, J. Smith and G. Leusink, *Applied Physics Letters Materials* 6 (5), 058203 (2018).
10. G. N. Parsons and R. D. Clark, *Chem. Mater.* 32 (12), 4920-4953 (2020).
11. S. M. George, *Chem. Rev.* 110 (1), 111-131 (2010).
12. A. Mackus, A. Bol and W. Kessels, *Nanoscale* 6 (19), 10941-10960 (2014).
13. A. J. M. Mackus, M. J. M. Merckx and W. M. M. Kessels, *Chem. Mater.* 31 (1), 2-12 (2019).
14. X. Jiang and S. F. Bent, *J. Phys. Chem. C* 113 (41), 17613-17625 (2009).

15. E. Färm, M. Vehkamäki, M. Ritala and M. Leskelä, *Semiconductor Science and Technology* 27 (7), 074004 (2012).
16. T.-L. Liu and S. F. Bent, *Chem. Mater.* 33 (2), 513-523 (2021).
17. I.-K. Oh, T. E. Sandoval, T.-L. Liu, N. E. Richey and S. F. Bent, *Chem. Mater.* 33 (11), 3926-3935 (2021).
18. A. Marnett, M. J. M. Merks, B. Karasulu, F. Roozeboom, W. M. M. Kessels and A. J. M. Mackus, *ACS Nano* 11 (9), 9303-9311 (2017).
19. R. C. Longo, S. McDonnell, D. Dick, R. M. Wallace, Y. J. Chabal, J. H. Owen, J. B. Ballard, J. N. Randall and K. Cho, *Journal of Vacuum Science & Technology B* 32 (3), 03D112 (2014).
20. S. E. Atanasov, B. Kalanyan and G. N. Parsons, *J. Vac. Sci. Technol. A* 34 (1), 01A148 (2016).
21. B. Groven, Y. Tomczak, M. Heyns, I. Radu, and A. Delabie, *J. Appl. Phys.* 128, 175302 (2020).
22. X. Chen, Y. J. Park, T. Das, H. Jang, J.-B. Lee and J.-H. Ahn, *Nanoscale* 8 (33), 15181-15188 (2016).
23. S. F. Bartolucci, D. Kaplan and J. A. Maurer, *2D Materials* 4 (2), 021017 (2017).
24. W. Ahn, H. Lee, H. Kim, M. Leem, H. Lee, T. Park, E. Lee and H. Kim, *Phys. Status Solidi RRL* 15 (2), 2000533 (2021).
25. A. U. Mane, S. Letourneau, D. J. Mandia, J. Liu, J. A. Libera, Y. Lei, Q. Peng, E. Graugnard and J. W. Elam, *J. Vac. Sci. Technol. A* 36 (1), 01A125 (2017).
26. J. Soares, S. Letourneau, M. Lawson, A. U. Mane, Y. Lu, Y. Wu, S. M. Hues, L. Li, J. W. Elam and E. Graugnard, *J. Vac. Sci. Technol. A* 40 (6), 062202 (2022).



This is the author's peer reviewed, accepted manuscript. However, the online version of record will be different from this version once it has been copyedited and typeset.  
PLEASE CITE THIS ARTICLE AS DOI: 10.1116/6.0002811

This is an author-produced, peer-reviewed version of this article. The final, definitive version of this document can be found online at *Journal of Vacuum Science and Technology A*, published by American Institute of Physics. Copyright restrictions may apply. <https://doi.org/10.1116/6.0002811>

27. M. Lawson, E. Graugnard and L. Li, *Appl. Surf. Sci.* 541, 148461 (2021).
28. W. L. Gladfelter, *Chem. Mater.* 5 (10), 1372-1388 (1993).
29. A. Dillon, A. Ott, J. Way and S. George, *Surf. Sci.* 322 (1-3), 230-242 (1995).
30. R. L. Puurunen, *Journal of Applied Physics* 97 (12) (2005).
31. R. A. Wind and S. M. George, *J. Phys. Chem. A* 114 (3), 1281-1289 (2010).
32. A. M. Hoyas, C. Whelan, J. Schuhmacher, J. Celis and K. Maex, *Electrochemical and Solid-State Letters* 9 (7), F64 (2006).
33. K. M. Chang, S. W. Wang, C. H. Li, J. Y. T. J. Y. Tsai and T. H. Y. T. H. Yeh, *Jpn. J. Appl. Phys.* 35 (12S), 6555 (1996).
34. P. C. Lemaire, M. King and G. N. Parsons, *J. Chem. Phys.* 146 (5), 052811 (2017).
35. S. Letourneau, M. J. Young, N. M. Bedford, Y. Ren, A. Yanguas-Gil, A. U. Mane, J. W. Elam and E. Graugnard, *ACS Appl. Nano Mater.* 1 (8), 4028-4037 (2018).
36. H. Li, Q. Zhang, C. C. R. Yap, B. K. Tay, T. H. T. Edwin, A. Olivier and D. Baillargeat, *Adv. Funct. Mater.* 22 (7), 1385-1390 (2012).
37. M. F. Vos, S. N. Chopra, M. A. Verheijen, J. G. Ekerdt, S. Agarwal, W. M. Kessels and A. J. Mackus, *Chem. Mater.* 31 (11), 3878-3882 (2019).
38. S. K. Song, H. Saare and G. N. Parsons, *Chem. Mater.* 31 (13), 4793-4804 (2019).
39. H. Saare, S. K. Song, J.-S. Kim and G. N. Parsons, *J. Appl. Phys.* 128 (10), 105302 (2020).
40. R. Vallat, R. Gassilloud, B. Eycheenne and C. Vallée, *J. Vac. Sci. Technol. A* 35 (1), 01B104 (2017).
41. J. Soares, A. U. Mane, D. Choudhury, S. Letourneau, S. M. Hues, J. W. Elam and E. Graugnard, *Chem. Mater.* 35 (3), 927-936 (2023)

## Figure Captions

FIG. 1. X-ray photoelectron spectroscopy scans on a variety of substrate surfaces measuring photo-emitted electron intensities in the Mo 3d region after 22 MoS<sub>2</sub> cycles at 200 °C and annealing at 650 °C for 30 min. Spectra are offset vertically for clarity. These data enable identification of surfaces that either promote (HfO<sub>2</sub> and Al<sub>2</sub>O<sub>3</sub>) or inhibit (SiN<sub>x</sub>, SiO<sub>x</sub>N<sub>y</sub> and thermal oxide SiO<sub>2</sub>) MoS<sub>2</sub> nucleation.

FIG. 2. Integrated area of XPS Mo 3d peak region as a function of MoS<sub>2</sub> ALD cycles for a variety of substrates. All substrates were prepared with 20 cycles of MoS<sub>2</sub> ALD at 200 °C. Integrated area was calculated after peak fitting the Mo 3d region (excluding the overlapping S 2s spectra).

FIG. 3. Calculated selectivity parameter as a function of MoS<sub>2</sub> ALD cycles at 200 °C for blanket substrates that promote or inhibit MoS<sub>2</sub> growth. The selectivity was calculated based on integrated XPS Mo concentrations.

FIG. 4. (a) Raman line scans across the template substrates containing both growth and non-growth regions. Intensity is measured by crystalline MoS<sub>2</sub> A<sub>1g</sub> peak area. Clear indication of crystalline MoS<sub>2</sub> can be identified on all growth areas. (b) Example optical image of a patterned Al<sub>2</sub>O<sub>3</sub> / TO region. The dashed line approximates the region of the line scan across the template. Samples were prepared with 20 cycles of MoS<sub>2</sub> ALD at 200 °C followed by annealing in H<sub>2</sub>S at 650 °C for 30 min.

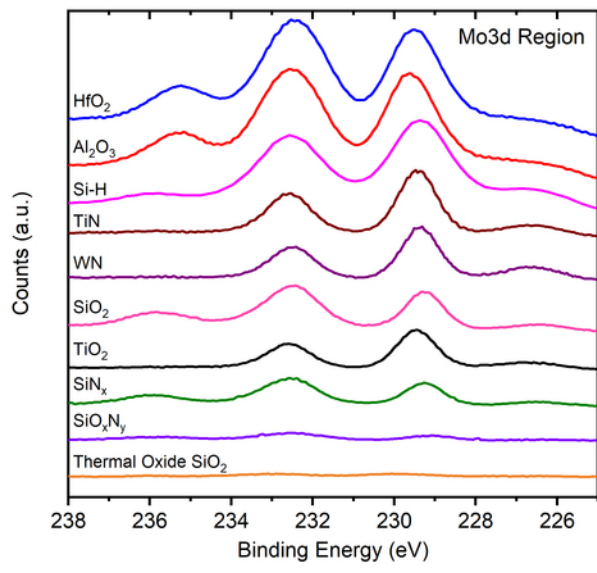
FIG. 5. Time-of-flight secondary ion mass spectrometry maps of alumina / TO template following 20 MoS<sub>2</sub> ALD cycles at 200 °C. Maps show clear selectivity of Mo within the

patterned alumina growth area. Essentially no Mo is present on the non-growth thermal oxide area.

FIG. 6. Integrated area of XPS Mo 3d peak region as a function of total MoS<sub>2</sub> ALD cycles for thermal oxide and Al<sub>2</sub>O<sub>3</sub> substrates. The incorporation of etching steps is shown to decrease the amount of Mo present after a total of 20 and 30 ALD cycles. Dashed lines indicate growth that integrated supercycles of deposition and etching. Solid lines indicate ASALD without ALE supercycles.

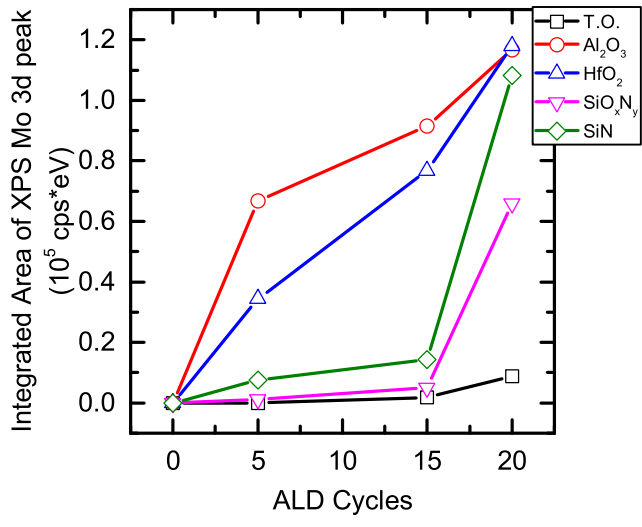


This is the author's peer reviewed, accepted manuscript. However, the online version of record will be different from this version once it has been copyedited and typeset.  
PLEASE CITE THIS ARTICLE AS DOI: 10.1116/6.0002811



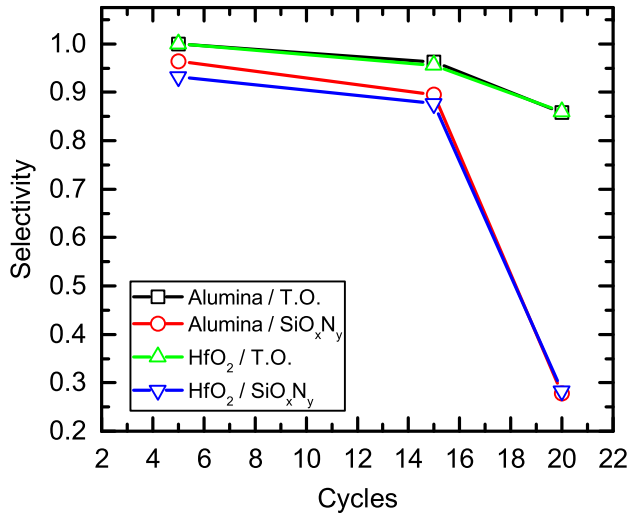
This is an author-produced, peer-reviewed version of this article. The final, definitive version of this document can be found online at *Journal of Vacuum Science and*

This is the author's peer reviewed, accepted manuscript. However, the online version of record will be different from this version once it has been copyedited and typeset.  
PLEASE CITE THIS ARTICLE AS DOI: 10.1116/6.0002811



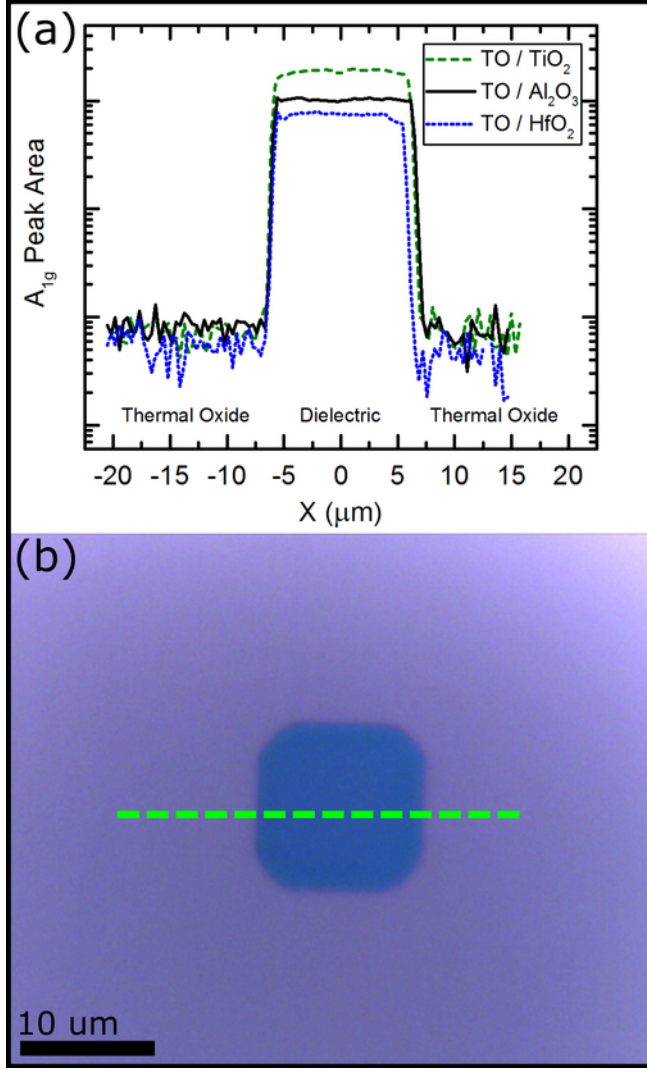
This is an author-produced, peer-reviewed version of this article. The final, definitive version of this document can be found online at *Journal of Vacuum Science and*

This is the author's peer reviewed, accepted manuscript. However, the online version of record will be different from this version once it has been copyedited and typeset.  
PLEASE CITE THIS ARTICLE AS DOI: 10.1116/6.0002811



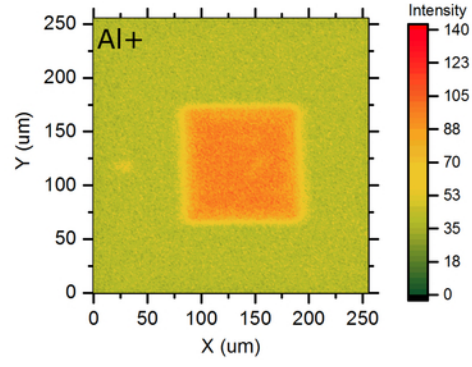
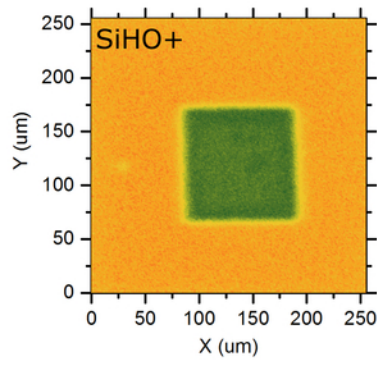
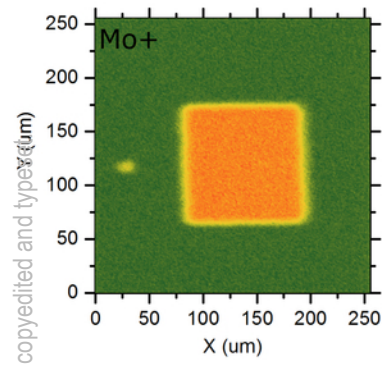
This is an author-produced, peer-reviewed version of this article. The final, definitive version of this document can be found online at *Journal of Vacuum Science and*

This is the author's peer reviewed, accepted manuscript. However, the online version of record will be different from this version once it has been copyedited and typeset.  
PLEASE CITE THIS ARTICLE AS DOI: 10.1116/6.0002811



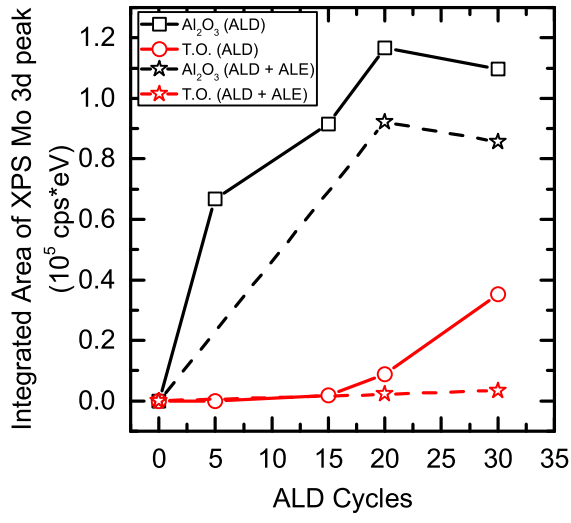
This is an author-produced, peer-reviewed version of this article. The final, definitive version of this document can be found online at *Journal of Vacuum Science and*

This is the author's peer reviewed, accepted manuscript. However, the online version of record will be different from this version once it has been copyedited and typeset.  
PLEASE CITE THIS ARTICLE AS DOI: 10.1116/6.0002811



This is an author-produced, peer-reviewed version of this article. The final, definitive version of this document can be found online at *Journal of Vacuum Science and Technology A*, published by American Institute of Physics. Copyright restrictions may apply.

This is the author's peer reviewed, accepted manuscript. However, the online version of record will be different from this version once it has been copyedited and typeset.  
PLEASE CITE THIS ARTICLE AS DOI: 10.1116/6.0002811



This is an author-produced, peer-reviewed version of this article. The final, definitive version of this document can be found online at *Journal of Vacuum Science and*